Clim Dyn (2015) 45:3547–3562
DOI 10.1007/s00382-015-2556-7

Impact of the winter North Atlantic Oscillation (NAO) on the Western Pacific (WP) pattern in the following winter through Arctic sea ice and ENSO. Part II: multi-model evaluation of the NAO–ENSO linkage

Tetsu Nakamura[1,2] · Masayuki Hara[3] · Miki Oshika[4] · Yoshihiro Tachibana[4]

Received: 19 May 2014 / Accepted: 10 March 2015 / Published online: 31 March 2015

Abstract A 1-year-lagged relationship between the North Atlantic Oscillation (NAO) in winter and El Niño/Southern Oscillation (ENSO) in the following year was examined with a multi-model ensemble analysis using Coupled Model Intercomparison Project phase 3 models. A coherency index was developed as a measure of the coherence between the NAO and ENSO in each model and used as a weighting factor in the ensemble model. Weighted multi-model ensemble means of the regressed field on the maximum covariance analysis coefficients between the surface pressure field in the North Atlantic (NAO field) and the sea surface temperature field in the equatorial Pacific (ENSO field) were explored. The results indicated that when the wintertime NAO was in its negative (positive) phase, anomalous atmospheric circulation associated with a large (small) Eurasian snow mass anomaly intensified (weakened) the Asian cold surge and the westerly wind burst (WWB) in the warm pool region. Intensification of the WWB initiates El Niño. A sensitivity experiment using an idealized dry general circulation model revealed that the atmospheric response to anomalous, near-surface cooling associated with an anomalous Eurasian snow mass induced higher surface pressure near the Tibetan plateau and thus intensified the Asian cold surge and WWB. Linear regression analyses applied to the reanalysis data strongly supported the model results. Our results therefore suggest an influence of the NAO on the initiation of El Niño via a process that involves Eurasian snow anomalies associated with the NAO phase.

Keywords ENSO · Multi-model ensemble analysis · NAO · WP

✉ Yoshihiro Tachibana
tachi@bio.mie-u.ac.jp

[1] National Institute of Polar Research, Tachikawa, Japan

[2] Hokkaido University, Sapporo, Japan

[3] Japan Agency for Marine-Earth Science and Technology, Yokohama, Japan

[4] Climate and Ecosystems Dynamics Division, Graduate School of Bioresources, Mie University, Tsu, Japan

1 Introduction

In a companion paper, Oshika et al. (2014) (hereafter Part I) have shown observational evidence of relationships between the North Atlantic Oscillation (NAO), El Niño/Southern Oscillation (ENSO), and the Western Pacific pattern (WP) through statistical analyses of a 51-year (1960–2010) reanalysis dataset. The analysis revealed a roughly 1-year-lagged negative correlation between the NAO, WP, and ENSO. Specifically, when a negative (positive) phase of the NAO occurs in December, a warm (cold) ENSO phase occurs in the following year sometime in the summer-to-winter time interval, and a positive (negative) phase of the WP occurs in the following December. These results imply that the NAO can be used to predict monthly mean weather during the following winter in the Asian Far East. Because positive (negative) WP patterns are associated with warm (cold) ENSO phases (Horel and Wallace 1981), the linkage between the NAO and ENSO the following year is important for predictive purposes. To confirm the proposed processes shown in Part I, we performed a multi-model ensemble analysis in Part II using the Coupled Global Climate Model (CGCM) from the Coupled Model Intercomparison Project phase 3 (CMIP3) of the World Climate Research Programme (Meehl et al. 2007; Randall et al. 2007) as a counterpart of Part I.

Previous studies have demonstrated a significant cause-and-effect relationship between atmospheric circulation anomalies over the North Atlantic and ENSO events (e.g., Enfield and Mayer 1997; Klein et al. 1999; Saravanan and Chang 2000) through Pacific/North Atlantic (PNA) teleconnection patterns (Wallace and Gutzler 1981) or stratospheric pathways (Scaife et al. 2005; Cagnazzo and Manzini 2009). Such influences of tropical atmospheric phenomena on the mid- and high-latitudes have been well studied. On the other hand, some previous studies have reported possible influences of atmospheric teleconnections in the mid- and high-latitudes on the initiation of ENSO (e.g., Nakamura et al. 2006, 2007; Wang et al. 2011; Ham et al. 2013; Chen et al. 2014). Some processes that connect mid- and high-latitude variations with the tropics have been hypothesized. For example, a significant connection between the NAO and Madden Julian Oscillation (MJO) on intra-seasonal timescales has been demonstrated (i.e., Cassou 2008, Lin et al. 2009). Because the MJO is one of the important external forcings for ENSO outbreaks (i.e., Zavala-Garay et al. 2005), a linkage between the NAO and MJO might explain an indirect influence of the mid- and high-latitudes on the initiation of ENSO. However, some studies have suggested that there is a direct influence of mid- and high-latitude variations on ENSO. For example, Wang et al. (2011) have shown that cold sea surface temperature (SST) anomalies during the summer in the North Atlantic cause a pattern of atmospheric teleconnections that intensifies the Asian winter monsoon. Associated cyclonic anomalies at off-equator locations then produce the equatorial westerly winds that initiate El Niño. Nakamura et al. (2006, 2007) have shown that the Asian cold surge associated with the Arctic Oscillation (AO) (Thompson and Wallace 1998) in the late winter often triggers an ENSO in the following winter by modulating the westerly wind burst (WWB) over the maritime continent. Many studies have reported observational evidence that the Asian cold surge excites a WWB over the maritime continent (e.g., Yu and Rienecker 1998; Yu et al. 2003; Nakamura et al. 2007). A WWB is one of the most important triggers for initiation of an ENSO (Seiki et al. 2011). For example, an oceanic equatorial Kelvin wave is initiated by a WWB (Giese and Harrison 1990; Kindle and Phoebus 1995). Because El Niño tends to be initiated in the spring (Philander 1985), the Asian cold surge and its associated WWB intensification in the late winter or early spring are key components of the explanation of the remote influence of extra-tropical atmospheric variations on ENSO. In contrast, some studies have reported a relationship between Eurasian snow cover and ENSO (e.g., Barnett et al. 1989; Yasunari 1987, Yasunari et al. 1991). The NAO during the winter is strongly related to western Eurasian snow cover (Hori and Yasunari 2003). Eurasian snow cover may also be a key to understanding the relationship between the NAO and ENSO. In Part I, we have also demonstrated a significant impact of the winter NAO on tropical atmospheric circulation over the maritime continent via the response of Rossby waves to surface cooling caused by the Eurasian snow cover anomaly.

We have reported observational evidence of relationships between the NAO, ENSO, and WP in Part I. As a counterpart of Part I, in this paper we carried out a numerical modeling study. The extent of the agreement between the numerical model results and observations facilitates identification of the mechanism that links the NAO during the winter with ENSO during the following year. The final goal of this study was to identify the mechanism that may connect the NAO, ENSO, and WP. On the basis of the aforementioned hypothesized processes, we especially focused on the role of the Eurasian snow anomaly. This focus was motivated by the fact that simulated snow behavior is strongly model dependent, and its impacts on atmospheric variations due to the thermal dynamics associated with surface cooling, snow falling, and snow melting has not yet been established (e.g., Roesch 2006; Peings and Douville 2010). Examining the influence of the reproducibility of the simulated snow on the NAO–ENSO relationship is therefore a valuable exercise. In the case of a relationship with a 1-year time lag between locations as spatially and temporally remote as Europe and the tropical Pacific, numerical model experiments are useful for elucidating the nature of the relationship and providing insights into the physical processes that underlie the relationship. Because a coupled atmosphere–ocean climate model is required to simulate the evolution of ENSO, we used the products of the coupled atmosphere–ocean climate models from the CMIP3 of the World Climate Research Programme (WCRP) (Meehl et al. 2007; Randall et al. 2007) in the present study to confirm the observational evidence. Comparison of the results of the many models with observations provided a rigorous test of the hypothesized mechanisms. In CMIP3, there are considerable model dependencies of the spatial patterns and time scales of both the NAO and ENSO. For example, the southern part of the center of activity of the NAO in the CMIP3 models has a general tendency to be displaced westward (Stoner et al. 2009; Handorf and Dethloff 2012). In the case of ENSO, some of the CMIP3 models reproduce the features of the observed ENSO transitions, but most models fail to reproduce transitional processes during both the warm and cold ENSO phases (Ohba et al. 2010). Therefore, even if the physical processes that link the NAO with ENSO are reproduced well in each model, it is difficult to demonstrate a relationship between the NAO and ENSO consistent with observations by uniform application of conventional methods such as the SST anomaly in Niño regions or the difference in sea level pressure between fixed geographical locations such as

Lisbon and Reykjavik (NAO) or Tahiti and Darwin (Southern Oscillation Index). Because the CMIP3 models behave differently, examination of the linkages between the NAO and ENSO with these models should take into account the maximum variance of each model's interannual variability. We therefore developed a new index, the Coherency Index (CI), which indicates the degree of coherence between two dominant patterns. We applied the CI to the results of the multi-model ensemble of the coupled atmosphere–ocean climate models from the CMIP3 dataset. Application of the CI to the CMIP3 multi-model results enabled us to distinguish the models that simulated the relationship between the winter NAO and the subsequent ENSO from the models that failed to simulate a NAO–ENSO relationship. Furthermore, this analysis enabled us to calculate a weighted, multi-model ensemble mean. The weighted ensemble mean of the multi-model results gave us physical information about the connection between the NAO and ENSO. On the basis of previous studies and the results of Part I, we examined the role of the Eurasian snow anomaly on the NAO–ENSO relationship. In particular, we examined the impact of the behavior of the Eurasian snow simulated by the CMIP3 models on the NAO–ENSO relationship. Furthermore, we performed an idealized experiment using a simplified atmospheric general circulation model (GCM) to examine the atmospheric responses to the Eurasian snow cover anomalies. The results of that experiment are discussed and compared with the CMIP3 results.

Table 1 List of models used in this study. The second column describes the WWB–ENSO lag relationship shown by Seiki et al. (2011)

Model name	WWB-ENSO relationship	CI (Nov/Dec/Jan/Feb)
BCCR-BCM2.0		–0.46/–0.71/–0.02/–0.63
CNRM-CM3	Acceptable	0.39/**0.59**/–0.13/–0.08
CSIRO-Mk3.0	Acceptable	0.49/**0.68**/**0.66**/0.17
CSIRO-Mk3.5		–0.19/–0.42/**0.54**/**0.80**
ECHAM5/MPI-OM		**0.72**/**0.72**/0.35/–0.77
FGOALS-g1.0		–0.64/0.00/0.38/**0.52**
GFDL-CM2.1	Good	**0.64**/–0.29/0.01/–0.54
GISS-AOM		–0.48/0.13/**0.51**/0.29
INGV-ECHAM4		**0.61**/–0.18/0.46/–0.05
INM-CM3.0		–0.46/–0.81/–0.25/**0.60**
IPSL-CM4	Good	**0.56**/–0.13/0.44/0.47
MIROC3.2 (medres)		0.47/**0.66**/0.38/**0.63**
MRI-CGCM2.3.3	Good	**0.70**/**0.73**/0.38/–0.02
NCAR-CCSM3.0		–0.63/0.47/0.43/**0.50**
NCAR-PCM1		0.35/–0.70/**0.74**/**0.63**
UKMO-HadGEM1		–0.55/0.09/0.42/**0.80**
Observation[a]		–0.51/**0.62**/0.28/–0.49

"Good" indicates that the WWB precedes the ENSO with a time lag of several months (2–10 months). "Acceptable" indicates that the WWB precedes the ENSO, but the time lag is only 1 month. CI values of the corresponding NAO month (November/December/January/February) are shown in the third column. Numbers in bold font exceed the criterion of 0.5

[a] CI applied to the surface pressure field of the NCEP/NCAR reanalysis and SST field of the HadISST for the period 1960–2010

2 Data

The CMIP3 models used in this study are listed in Table 1. We chose 16 models, the output of which included surface temperature (SST in the ocean) and surface pressure (Ps), which are required for calculating the CI (details in Sect. 3.1). We analyzed 100-year output records of the "Climate of the twentieth century" (scenario 20C3M) run of the 16 models. For each of the models, we used only one ensemble member (i.e., run1). We used monthly mean fields for the period 1901–2000. A 5-year, high-pass filter was initially applied to all data to avoid spurious or unwanted correlations between the NAO and ENSO caused by long-term trends.

To verify that our CI provided an accurate indication of the coherency between the NAO and ENSO, we also applied the CI calculation to the Ps values from the National Centers for Environmental Prediction (NCEP) and National Center for Atmospheric Research (NCAR) reanalysis dataset (Kalnay et al. 1996) and to the SST from the Hadley Centre Sea Ice and Sea Surface Temperature dataset (HadISST) for the period 1961–2010. The snow depth data from 1979 through 2010 in the Japan Meteorological Agency Climate Data Assimilation System reanalysis (JCDAS) (Onogi et al. 2007) were also used. All these are the same as the data used in Part I. We initially applied a 5-year, high-pass filter to those data.

3 Methods

3.1 Coherency index (CI)

As mentioned in the introduction, reproducibility of teleconnection patterns strongly depends on the performance of each GCM. The reproducibility of each teleconnection pattern does not guarantee the reproducibility of the relationship (i.e., coherency) between teleconnection patterns. We developed the CI to objectively examine the performance of the relationships between teleconnection patterns, such as NAO and ENSO, in each GCM. This approach was essential when we analyzed the relationship between two teleconnection patterns using multi-model ensemble simulation results, such as CMIP3 data. In this section we

introduce the procedure for obtaining the CI and explain the physical meaning of the CI. Calculation of the CI requires the eigenvectors and singular vectors of two spatiotemporal matrices. First, we obtain the eigenvectors of the spatiotemporal matrices **A** for one field and **P** for the other field by use of empirical orthogonal functions (EOFs) (Von Storch and Zwiers 1999) as follows:

$$\mathbf{A}^T\mathbf{A} = \sum_{m=1}^{M} \lambda_{Am}\mathbf{X}_{Am}\mathbf{X}_{Am}^T \tag{1}$$

$$\mathbf{P}^T\mathbf{P} = \sum_{m=1}^{M} \lambda_{Pm}\mathbf{X}_{Pm}\mathbf{X}_{Pm}^T \tag{2}$$

where the superscript T denotes the transpose, $\mathbf{X}_m$ and λ_m are the eigenvector and eigenvalue of the mth pattern, respectively, and M is the total number of patterns. Next, we obtain the singular vector of the cross-covariance matrix of **A** and **P** by using a maximum-covariance analysis (MCA) method (Von Storch and Zwiers 1999) as follows:

$$\mathbf{A}^T\mathbf{P} = \sum_{m=1}^{M} \gamma_m\mathbf{Y}_{Am}\mathbf{Y}_{Pm}^T \tag{3}$$

where $\mathbf{Y}_m$ is the singular vector of the mth pattern corresponding to the fields denoted by subscripts A and P, and γ_m is the singular value of the mth pattern. In order to simplify the explanation, we discuss here only the primary pattern. Thus, $\mathbf{X}_A$ and $\mathbf{X}_P$ hereafter indicate the eigenvectors of the primary pattern (i.e., EOF1). Similarly, $\mathbf{Y}_A$ and $\mathbf{Y}_P$ indicate the spatial pattern of the maximum covariance, which is determined by maximizing the covariance between two MCA expansion coefficients, $\mathbf{T}_A$ and $\mathbf{T}_P$, i.e., respective time scores of $\mathbf{Y}_A$ and $\mathbf{Y}_P$. The time scores of $\mathbf{Y}_A$ and $\mathbf{Y}_P$, are obtained as follows:

$$\mathbf{T}_A = \mathbf{A}\mathbf{Y}_A \tag{4}$$

$$\mathbf{T}_p = \mathbf{P}\mathbf{Y}_P \tag{5}$$

The spatial correlation between the EOF1 and MCA indicates the similarity between them. The CI is defined as the multiplicative product of the spatial correlations of the two fields. That is,

$$\mathrm{CI} \equiv \left[(\mathbf{X}_A \cdot \mathbf{Y}_A) \Big/ \sqrt{(\mathbf{X}_A)^2(\mathbf{Y}_A)^2}\right]\left[(\mathbf{X}_P \cdot \mathbf{Y}_P) \Big/ \sqrt{(\mathbf{X}_P)^2(\mathbf{Y}_P)^2}\right] \tag{6}$$

Because the quantity in each angle bracket is normalized by the norm of EOF1 and MCA, CI must lie in the interval −1 to 1. It should be noted that we did not apply the equal-area weighting for both EOF and MCA. Chung and Nigam (1999) reported the dependency of the resultant patterns of the multivariate analysis on the weighting methods.

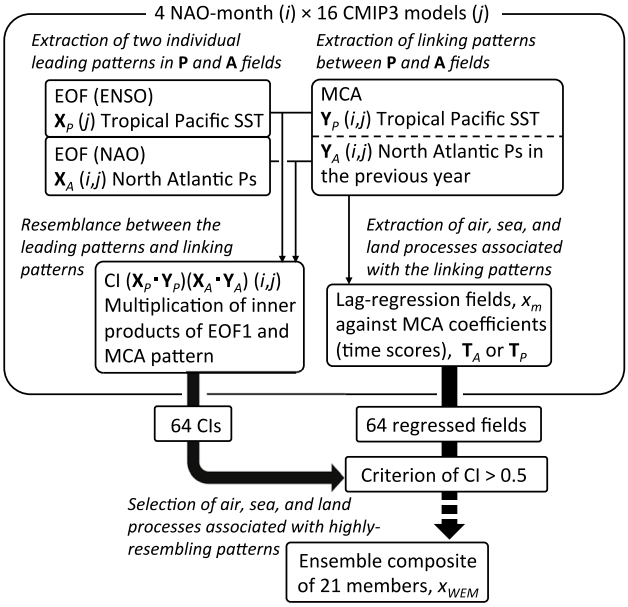

Fig. 1 A diagram showing the procedures for calculating the CI and WEM. Inside the largest *rectangle* labeled '4 NAO-month (i) × 16 CMIP3 models (j)' the procedures used to calculate the CI are depicted (Sect. 3.1). The procedures for calculating the WEM are depicted outside of that *rectangle* (Sect. 3.2)

Therefore, our result might be changed by applying the weighting method. However, validating which weighting method is more suitable is beyond of the focus of this study. We applied the CI to the Pacific SST and Atlantic Ps fields obtained from CMIP3 models. A procedure for applying the CI to CMIP3 models is diagramed in Fig. 1.

We defined **P** to be the time-dependent tropical Pacific SST field corresponding to ENSO (160°–270°E, 10°S–10°N, July through January). By the definition of the time-dependent, that is, not a single month or multi month average but the evolution of SST anomalies from July to January, EOF of **P** is expected to capture an ENSO-related signal, considering the development time scale of ENSO. Then the EOF1 of **P**, $\mathbf{X}_P$, showed an ENSO-like pattern for all 16 of the CMIP3 models (not shown). Spatial patterns, evolutions, peak longitudes, and peak times of the SST anomaly of EOF1 in the individual model were very similar to those shown by Ohba et al. (2010). We defined **A** to be the Atlantic Ocean Ps field corresponding to the NAO (60°W–30°E, 20°–90°N). We treated $\mathbf{X}_A$ and $\mathbf{X}_P$ differently because of the timeframe of the NAO. The EOF1 of **A**, $\mathbf{X}_A$, was calculated for each month during the winter: November, December, January, and February. Hereafter, these 4 months are referred to as NAO months. $\boldsymbol{X}_P$ showed a NAO-like pattern in all NAO months in all models (not shown). Next, we applied MCA to **P** and **A**. Note that because **A** was defined in each NAO month, a MCA

was carried out for four pairs of **P** and **A** for each model. Note furthermore that for this MCA, **P** lags **A** by about 1 year because of the observed 1-year lag between the NAO and ENSO. For example, **P** beginning from July in a certain year was paired with **A** in November of the previous year. As shown in Fig. 1, MCA was calculated for four NAO months of 16 CMIP3 models individually. We thus obtained 64 pairs of $\mathbf{Y}_P$ and $\mathbf{Y}_A$, and we calculated 64 CIs with Eq. (6). In this CI calculation, we initially arranged the phase of $\mathbf{X}_P$ ($\mathbf{X}_A$) to correspond to the warm (negative) phase of ENSO (NAO). The NAO and ENSO were apparent in the EOF1 of the Atlantic Ps ($\boldsymbol{X}_A$) and the Pacific SST ($\boldsymbol{X}_P$), respectively, in all models. A MCA elicited the spatial patterns with the most covariance between the North Atlantic Ps and the Pacific SST (precisely, obtained by maximizing the covariance between the expansion coefficients of the two fields). However, there is no guarantee that the most covariant pattern between the two fields (MCA pattern) is the same as the EOF1s of the two fields. Large positive values of the CI signify spatial similarity of the EOF1 to MCA pattern, the indication being that the covariance between the NAO and ENSO is the largest of all the covariant patterns between the Atlantic Ps and the Pacific SST. According to this procedure, a positive CI therefore indicates that El Niño (La Niña) tends to occur about 1 year after a negative (positive) phase of the NAO that occurs in a certain NAO month. A negative CI indicates that El Niño (La Niña) tends to occur about 1 year after the phase of the NAO that is opposite to the positive CI case. A CI near zero indicates that there is no linear relationship between the NAO and the subsequent ENSO. Thus, only a model with a positive CI can reproduce the observed, lagged relationship between the ENSO and NAO.

Figure 2 shows a histogram of the 64 CIs. The distribution of the CIs was skewed to the left, the indication being that the ensemble mean of all the NAO months/models revealed a relationship between ENSO and NAO that was similar to the observed relationship. We then defined the criterion for the weighted ensemble mean (details in the next paragraph) to be 0.5, which is the 66th percentile of the CI distribution. The CI values in the corresponding NAO month for the 16 models are shown in Table 1. At least one NAO month was highly coherent (CI > 0.5) between the NAO and the subsequent ENSO in all of the models, except for the BCCR-BCM2.0. We also applied the CI to the surface pressure of the NCEP/NCAR reanalysis and the SST of the HadISST in the period 1961–2000, shown by the open bars above the CMIP3 CIs in Fig. 2. The calculated CI was greater than 0.5 only in the case of the Atlantic Ps in December (0.62). This result is consistent with the observational evidence shown in Part I. We can therefore conclude that a highly positive CI indicates

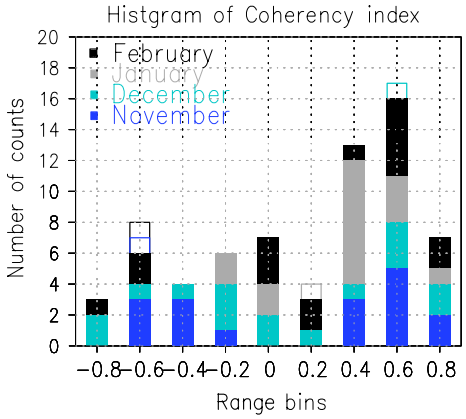

Fig. 2 Histogram of the CI values obtained from 64 pairs (4 months × 16 models) of **P** and **A**. *Colors* corresponding to the month of $\mathbf{X}_A$ are shown in the *upper left-hand corner* of the figure. Labels on the *horizontal axis* indicate the midpoints of the CI intervals, which have widths of 0.2. The *filled and open bars* indicate CI values obtained from the CMIP3 models and observations, respectively (details in the text and Table 1)

a 1-year-lagged relationship between the NAO and ENSO, which is similar to the observed relationship.

3.2 Linear regression analysis

We applied linear regression analysis to the outputs of the CMIP3 models. Atmospheric fields regressed onto the MCA coefficients were used to estimate the magnitude and statistical significance of the anomalous signals associated with both the NAO and ENSO. We calculated a weighted ensemble mean (WEM) of the regression coefficients. For a weighting factor, we used the CI, which is a measure of the coherence between the NAO and ENSO in the individual model described in Sect. 3.1. Furthermore, considering that only the models/NAO months with a high CI succeeded in reproducing the observed NAO–ENSO relationship, we required that CI be greater than 0.5 for inclusion in the WEM. The anomalous fields regressed onto the individual MCA coefficient $\mathbf{T}_A$, i.e., time score of $\mathbf{Y}_A$ (or $\mathbf{T}_P$, i.e., time score of $\mathbf{Y}_P$, in the cases of Fig. 3a and 4b) for which the CI was >0.5 (CIs in bold font in Table 1) were chosen for inclusion in the WEM (refer to Fig. 1). Twenty-one members were chosen in this manner. Statistical significance was estimated based on the standard deviation among the chosen members and was used to judge the robustness of the WEM of regression coefficients. We then calculated the regression coefficient and standard deviation of the WEM, x_{WEM} and σ_{WEM}, respectively, as follows:

$$x_{WEM} = \sum_{m=1}^{M} w_m x_m \Big/ \sum_{m=1}^{M} w_m, \quad w_m \geq 0.5 \tag{7}$$

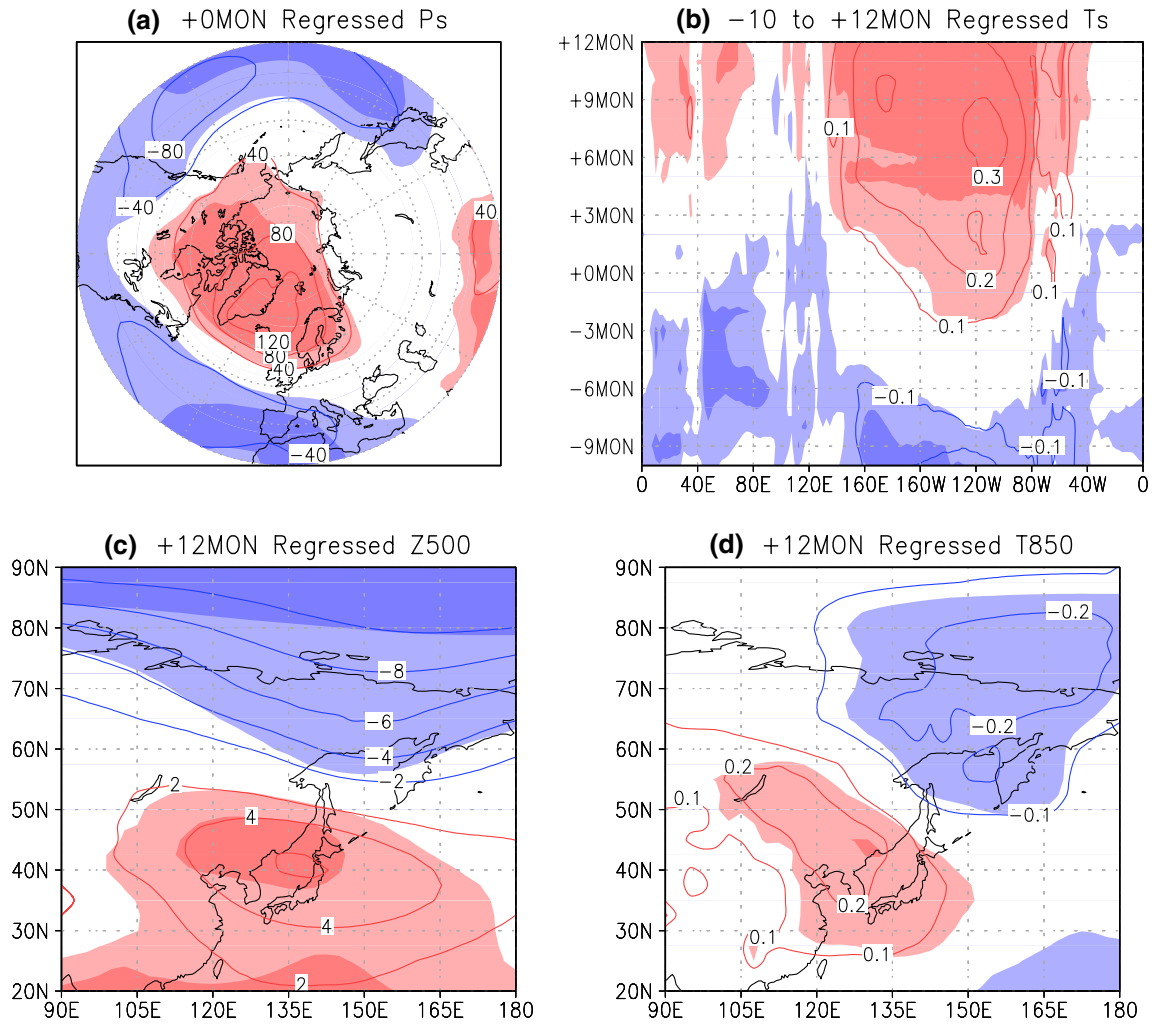

Fig. 3 **a** WEM of the surface pressure anomalies (Pa) coincident with the NAO month (+0MON). The anomalies were obtained from the fields by linear regressions on the $\mathbf{T}_P$ values. **b** Hovmöller diagram of the WEM of the surface temperature (K) averaged between 5°S and 5°N. The anomalies were obtained from the fields by linear regressions on the $\mathbf{T}_A$ values. The lead-lag month relative to the NAO month is indicated on the ordinate (i.e., −9MON and +12MON indicate 9 months before and 12 months after the NAO month, respectively). The abscissa is the longitude. **c** Same as *panel* (**a**), but for the Z500 fields (m) 12 months after (+12MON) the NAO month. The anomalies were obtained from the fields by linear regressions on the $\mathbf{T}_A$ value. **d** Same as *panel* (**c**), but for T850 fields (K). *Red* (*blue*) *color* indicates positive (negative) anomalies and light/heavy shading indicates anomalies exceeding 1.0/2.0 σ

$$\sigma_{WEM} = \sqrt{\sum_{m=1}^{M} w_m (x_m - x_{WEM})^2 \Big/ (M-1) \sum_{m=1}^{M} w_m}, \quad w_m \geq 0.5 \tag{8}$$

where x denotes the regression coefficient against the MCA coefficients ($\mathbf{T}_A$ or $\mathbf{T}_P$), M is the number of chosen members, 21, and w is the weight of a member, which was defined as the CI.

3.3 Nonlinear baroclinic model

On the basis of observations from previous studies (Barnett et al. 1989; Yasunari 1987, Yasunari et al. 1991; Part I), we examined the role of the Eurasian snow anomaly on the NAO–ENSO relationship. However, it is difficult to determine causality between the snow anomaly and atmospheric circulation by using nothing more than CMIP3 results, because snowfall is an internal variable in general circulation models (GCMs). We therefore performed an idealized experiment by using a nonlinear baroclinic model (NLBM) first introduced by Yasui and Watanabe (2010) to diagnose atmospheric responses to the anomalous cooling associated with the amount of Eurasian snow. Such an ideal experiment with a NLBM has been used widely in various studies (e.g., Kosaka et al. 2012). This model is a sort of dry atmospheric GCM (AGCM), in which the basic state is maintained by restoring temperature. Specifically, the

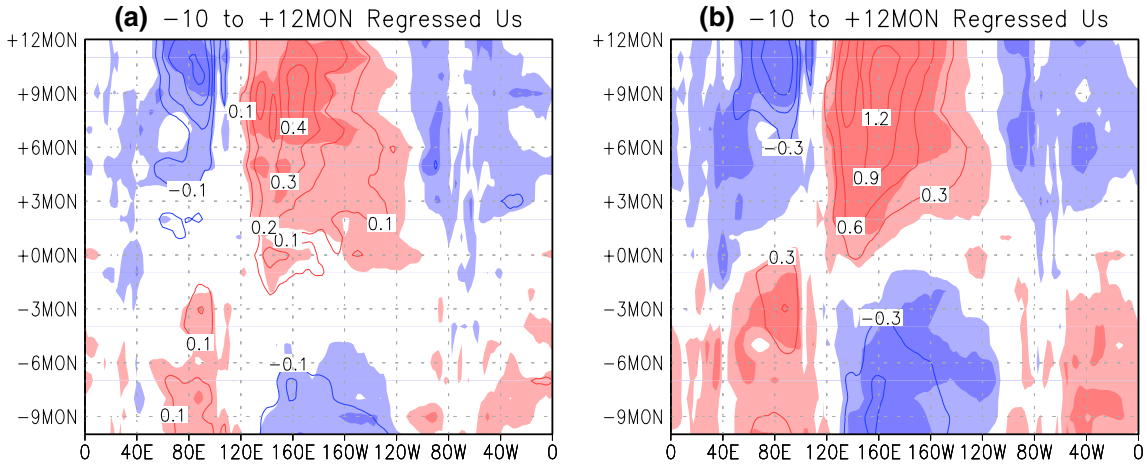

Fig. 4 **a** Same as Fig. 3b, but for the zonal wind fields (m s^{-1}). **b** Same as *panel* (**a**), but for the regression fields on the $\mathbf{T}_P$

temperature is nudged toward a given basic state by Newtonian cooling with a time constant of 10 days. Experiments were performed using this NLBM with a horizontal resolution of T42 and 20 σ vertical layers. The model top was 0.008 σ (about 30 km). A control (*CNTL*) run was initialized with the FMA (3-month average in February, March, and April) climatology of the NCEP/NCAR reanalysis for the period 1961–2000. The temperature of the basic state was identical to the climatological temperature. Anomaly (*ANOM*) runs were the same as the *CNTL*, except that steady anomalous cooling was specified for the European region (see details in Sect. 4.2). Output of the first 30 days of integration of each run was analyzed. The difference between the *ANOM* and *CNTL* was defined to be the atmospheric response to the Eurasian snow anomalies.

4 Results

4.1 CMIP3 multi-model ensemble

First, we show the WEM of the regression coefficients of Ps and SST used for the CI calculation versus the MCA coefficients. Figure 3a shows the WEM of surface pressure anomalies coincident with the NAO month regressed on the MCA coefficients, $\mathbf{T}_P$ (i.e., a heterogeneous pattern normally used in MCA). A dipole pattern corresponding to the negative phase of the NAO is clearly apparent. Figure 3b shows the evolution of the WEM of the equatorial SST anomalies from 10 months before to 1 year after the NAO month regressed on the MCA coefficients, $\mathbf{T}_A$. Warm anomalies begin at 100°W, coincident with the NAO month, and extend over the equatorial Pacific by 1 year after the NAO month. This evolution of anomalous SST fields corresponds well with El Niño. Figure 3c shows the WEM of geopotential height anomalies at 500 hPa (Z500) 1 year after the NAO month regressed on $\boldsymbol{T}_A$. Figure 3d is the same as Fig. 3c, but for the temperature anomalies at 850 hPa (T850). A meridional dipole pattern of Z500 between mid- and high-latitudes and corresponding temperature anomalies in the lower troposphere are obvious around the Far East. The resultant Z500 pattern one year after the NAO month is somewhat similar to the positive phase of the observed WP pattern, but its southern and northern center of action are shifted northward compared with the conventional WP pattern (Wallace and Gutzler 1981). The pattern is actually more similar to the observed WP pattern linked with the NAO in the previous year and concurrent ENSO (refer to Fig. 7 in Part I), except that the northern center of action is shifted northward. The lead-lag relationships among the anomalous fields of surface pressure, SST, Z500, and T850, is consistent with observed relationships, as shown in Part I. Specifically, El Niño (La Niña) and the associated positive (negative) phase of the WP tend to occur about 1 year after a negative (positive) phase of the NAO.

We next show the evolution of the equatorial wind fields, which may contribute to the initiation of El Niño. Figure 4a, b show the evolution of the WEM of equatorial surface zonal wind anomalies regressed on $\mathbf{T}_A$ and $\mathbf{T}_P$, respectively. Westerly wind anomalies begin in the western tropical Pacific around 150°E from zero to two months after the NAO month. These anomalies extend to the east by 1 year after the NAO month. The initiation of El Niño is known to be often triggered in the boreal spring by a westerly wind burst in the western tropical Pacific Ocean. We hypothesized that atmospheric variability associated with the NAO during the winter might intensify the background westerly winds in the western tropical Pacific region. Figure 5a shows surface temperature anomalies 1 month

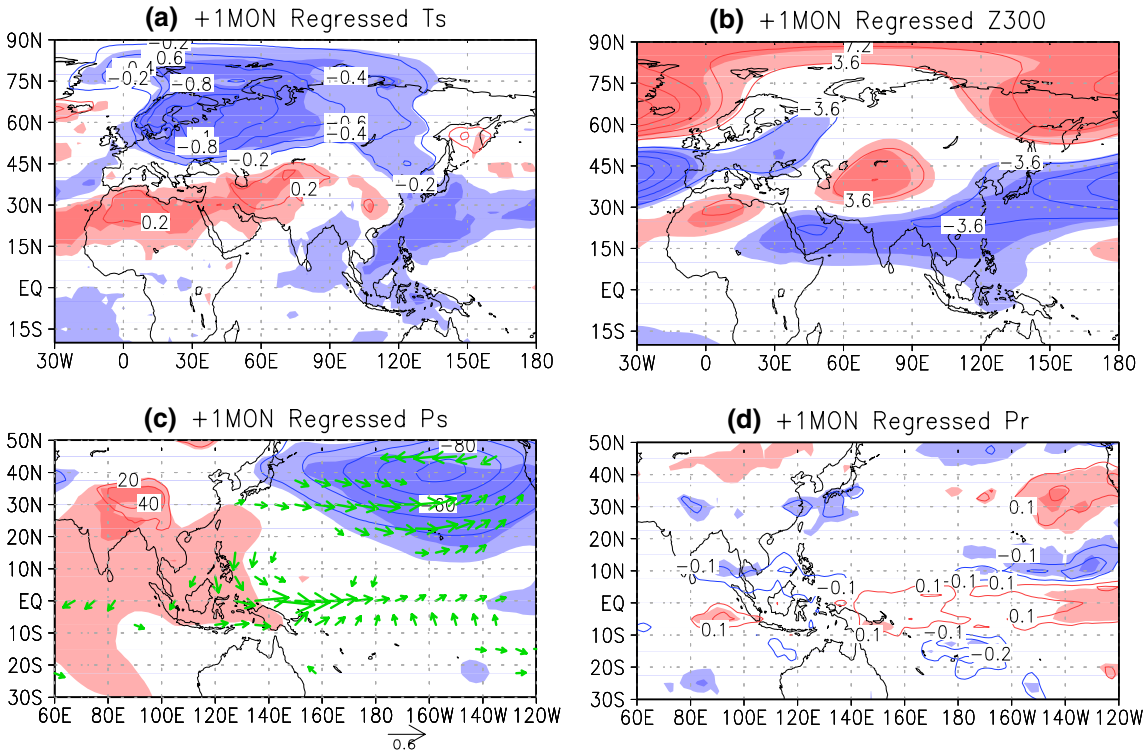

Fig. 5 WEM of the **a** surface temperature (Ts; K), **b** geopotential height at 300 hPa (Z300; m), **c** surface pressure (Ps; Pa), and **d** precipitation (Pr; mm day^{-1}) anomalies 1 month after (+1MON) the NAO month. The anomalies were obtained from the fields by linear regression on the $\mathbf{T}_A$ values. *Red* (*blue*) *color* indicates positive (negative) anomalies and light/heavy shading indicates anomalies exceeding 1.0/2.0 σ. *Green arrows* drawn in panel (**c**) indicate vectors of surface wind anomalies. An *arrow* with length corresponding to 0.6 m s^{-1} is drawn at the *lower right-hand corner* of the panel. Vectors in which any of the zonal or meridional components was <1.0 σ were ignored. Abscissa and ordinate are the longitude and latitude, respectively

after the NAO month. A cold anomaly was apparent over western Russia (around 30°E and 60°N), the North Indian Ocean (around 90°E and 10°N), and the western Pacific south of Japan (100–150°E and 10–30°N). Figure 5b shows the geopotential height anomaly at 300 hPa (Z300). Even 1 month after the NAO month, a dipole pattern associated with the negative phase of the NAO was apparent over the North Atlantic region. In association with the surface cold anomaly, a cyclonic anomaly was apparent over western Russia (30°E and 50°N). An anticyclonic anomaly over the Tibetan Plateau (75°E and 40°N) was likely a Rossby wave response to the cyclonic anomaly over western Russia. However, the amplitudes of these wave train-like patterns were quite small; the extremes were −3.6 m for the cyclonic anomaly over western Russia and 7.2 m for the anticyclonic anomaly over the Tibetan Plateau. These small amplitudes might reflect differences of the phase of the wave among ensemble members. High-pressure anomalies were apparent in the surface pressure field over the Tibetan plateau and south/southeast Asia (Fig. 5c). The surface wind anomalies indicated that the winds were northerly from 20°N to the equator around 130°E and westerly at the equator around 150°E. This wind pattern is likely one of the factors that initiates El Niño, because high-pressure anomalies over the Tibetan plateau intensify the Asian cold surge that intrudes into the tropics and its associated WWB (Yu and Rienecker 1998; Yu et al. 2003; Nakamura et al. 2007; Wang et al. 2011). Figure 5d shows precipitation anomalies (Pr). Positive anomalies were apparent over the tropical Pacific. Although the anomalies were insignificant with the exception of the eastern Pacific region, the positive Pr anomaly over the western tropical Pacific corresponds to atmospheric heating that induces a westerly wind anomaly accompanied by an off-equatorial cyclonic anomaly through a Matsuno–Gill type atmospheric response (Matsuno 1966; Gill 1980). The low significance of the Pr anomaly might be due to the large differences of the climatological Pr values among CMIP3 models. It is also noteworthy that anomalously low surface temperatures in the North Indian Ocean may contribute partly to the off-equatorial cyclonic anomalies over the tropical western Pacific (arrows in Fig. 5c) through an eastward propagating Kelvin wave (Xie et al. 2009), although temperature anomalies in the Indian Ocean were quite small (Fig. 5a).

The results of the ensemble mean of the regression fields suggest that near-surface cold anomalies over western

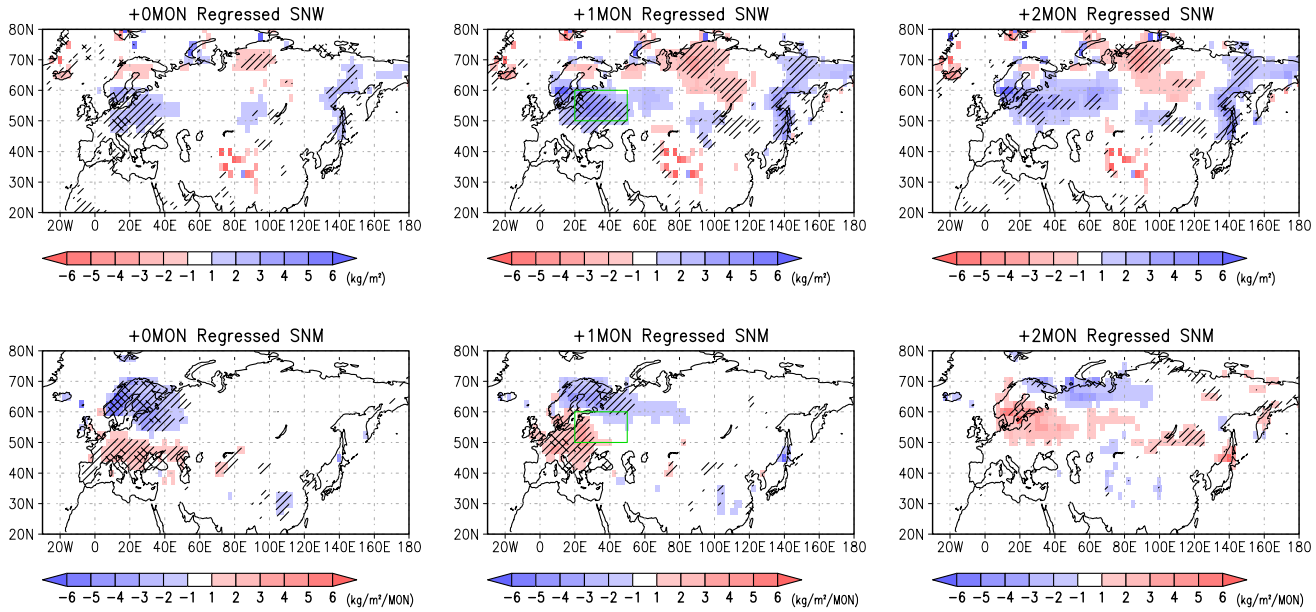

Fig. 6 (*Upper panels*) (*left*) Same as Fig. 3b, but for amount of snow (SNW; kg m^{-2}) during the same month (+0mon) as the NAO month. (*middle*) For amount of snow 1 month (+1mon) after the NAO month of $\mathbf{X}_A$. (*right*) For amount of snow 2 months after (+2mon) the NAO month of $\mathbf{X}_A$. (*bottom panels*) As in *top panels*, but for snow melting flux (SNM; kg m^{-2} mon^{-1}). *Hatched/double hatched* areas indicates anomalies exceeding 1.0/2.0 σ. Time series of area-averaged anomalies of snow amount/snow melting flux surrounded by *green lines* were used for calculation of correlation coefficients against $\mathbf{T}_A$ (see text and Fig. 7). It should be noted that *blue* (*red*) *color* indicates anomalously large (small) snow amount in the *upper panels* and anomalously small (large) melting of snow in the *bottom panels*

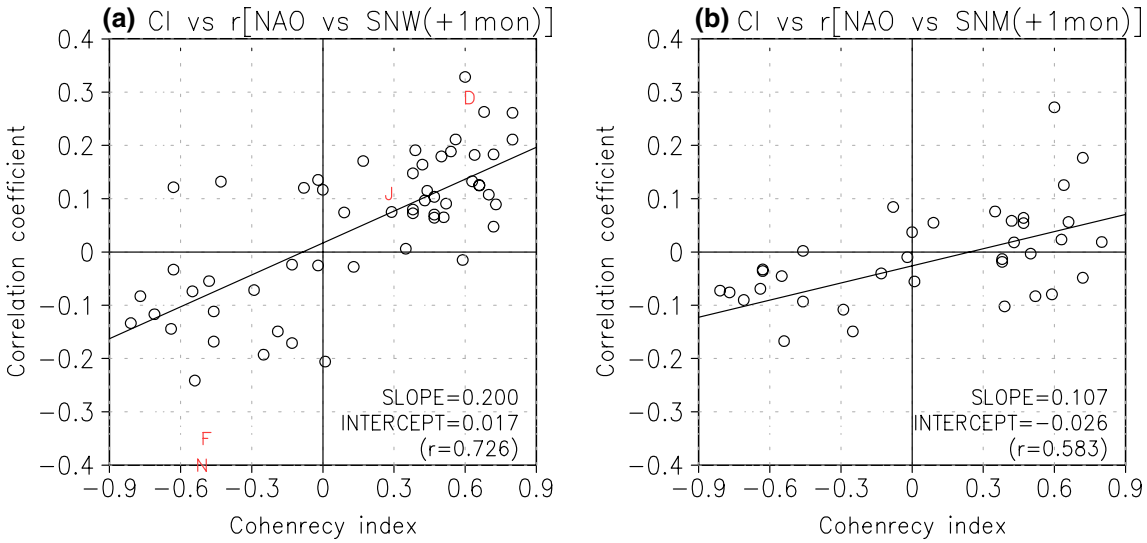

Fig. 7 **a** Scatter diagram of CI values versus correlation coefficients between $\mathbf{T}_A$ and amount of snow anomalies among 64 pairs (4 NAO months × 16 models). The amounts of snow anomalies were defined relative to an average over eastern Europe/western Russia (20°–50°E and 50°–60°N) and were lagged by 1 month (+1MON) to $\mathbf{T}_A$. Slope and y-intercept of a linear regression line and correlation coefficient among 64 pairs are displayed at the *bottom-right corner* of the panel. CI and correlation obtained from observation/reanalysis data are drawn as the initial character of the corresponding NAO-month with *red color*. **b** As in panel (**a**), but for snow melting flux

Russia may be a key factor in the NAO–ENSO linkage via formation or amplification of a wave train from the Atlantic Ocean to the Tibetan plateau. Figure 6 shows the evolution of the WEM of the extent of snow coverage (SNW) and snow melting flux (SNM) anomalies regressed on $\mathbf{T}_A$. The SNM indicates the rate of loss of the amount of snow due to snow melting over the land. Coincident with the NAO month, positive anomalies of SNW were found over

Europe (10–40°E and 45–60°N). This relationship is consistent with a previous report of the observed relationship between the NAO and Eurasian snow (Hori and Yasunari 2003). Positive and negative anomalies of the SNM were found south and north, respectively, of the SNW anomaly. These anomalies gradually moved to the northeast as the month advanced. This pattern reflects the fact that snow melting is associated with seasonal cycles; the NAO month is mainly relative to the middle of winter, and thus 1 or 2 months after the NAO month corresponds to late winter or early spring. Because positive anomalies of the SNM indicate heat transport from the atmosphere to the land, it is likely that the near-surface cold anomalies over western Russia result from the positive snow anomalies associated with the negative phase of the NAO.

We then examined the relationship between the model characterizations of the NAO–ENSO linkage quantified by the CI and NAO-snow linkage. We defined the NAO-snow linkage in terms of the correlation coefficients between $\mathbf{T}_A$ and snow amount/melting flux 1 month after the NAO month averaged over northern Europe and western Russia (20–50°E and 50–60°N). Figure 7a shows a scatter diagram of NAO-snow amount correlation coefficients versus the CIs among individual NAO months for the 16 models (i.e., 64 samples). Figure 7b shows the same as Fig. 7a, but for the NAO-snow melting correlations. In both cases, the correlation was positive and significant at $p < 0.01$ (when $r > 0.32$ for 64 samples), although the correlation coefficient was lower in the case of snow melting ($r = 0.583$) than in the case of snow amount ($r = 0.726$). This result indicates that a model that properly reproduces the association of the Eurasian snow anomalies with the NAO phase can also reproduce the evolution of El Niño after the negative phase of the NAO. Conversely, it can be said that a model that fails to reproduce the observed NAO-snow relationship cannot reproduce the observed NAO–ENSO relationship. Figure 7a also shows a scatter of observation based CI and NAO-snow linkage using snow amount of JRA25 (N, D, J, and F; the initial character of the corresponding NAO-month). NAO-snow linkage for the NAO in December shows high correlation (0.29) while the other months show lower correlations (−0.40 for November, 0.11 for January, and −0.35 for February). This is consistent with that in observations only December NAO correlates well with the following ENSO. These results are strongly supported by the observational evidence presented in Part I.

4.2 Ideal model experiment

The results based on the statistical analyses performed in Sect. 4.1 strongly suggest that there is an important association between Eurasian snow anomalies and the NAO that affects the NAO–ENSO relationship. However, the amplitudes of the negative Z300 anomaly over western Russia and the positive Z300 anomaly over the Tibetan Plateau only weakly support the contention that there is an atmospheric response to snow anomalies associated with the NAO. Therefore, we next performed an idealized experiment using the NLBM to clarify the atmospheric response to the snow anomaly and its influence on remote tropical atmospheric circulation. Based on the experimental design described in Sect. 3.3, anomalous forcing is required for the *ANOM* run. We defined the forcing that mimics the cold anomaly (Fig. 5a) due to a large snow anomaly (Fig. 6) to be the horizontal distribution and vertical profile of the cooling anomaly shown in Fig. 8. This anomalous forcing cooled the atmosphere constantly during the 30-day model run.

Figure 9a shows the 30-day average of the Z300 anomaly of the *ANOM* run compared to the *CNTL* run. Whereas cyclonic anomalies were apparent over northern Europe and western Russia (−75 m around 75°E, 60°N), there were anticyclonic anomalies with relatively weaker amplitudes northeast of the Tibetan plateau (+30 m around 100°E, 40°N). The corresponding wave activity flux, which is discussed by Takaya and Nakamura (2001) and is an indicator of the group velocity of the quasi-geostrophic Rossby wave, propagated like a Rossby wave from western Russia to the Tibetan plateau. Although there is inconsistency in the amplitudes and locations of the anomalies between the idealized model result (Fig. 9a) and the CMIP3 result (Fig. 5b), the idealized model indicates that Rossby wave activity originated in western Russia and propagated eastward across the Eurasian continent. Figure 9b shows a vertical cross section of the geopotential height anomaly and the corresponding flux of wave activity along the path of propagation of the stationary Rossby wave (brown line in Fig. 9a). The Rossby wave was generated near a surface wave source (around 30°E, below 0.5 σ) and propagated up-and-eastward. Downward propagation was apparent around the Tibetan plateau in association with an anticyclonic anomaly that extended toward the lower troposphere (110°E, below 0.5 σ). Figure 9c shows the geopotential height anomaly at 850 hPa and associated horizontal wind anomaly vectors. A high-pressure anomaly was apparent east of the Tibetan plateau (around 120°E, 30°N), and a northwesterly wind anomaly was apparent from the Asian continental region to the western equatorial Pacific (around 130°E, 0°–20°N). The resultant surface wind anomalies were not similar to the CMIP3 results shown in Fig. 5c and the observational evidence shown in Part I. However, the physical process might be at least qualitatively consistent with the CMIP3 and the observations, because these monthly mean surface wind anomalies might intensify higher frequency variabilities, namely, the Asian cold surges that intrude into the tropics and thus intensify the WWB over the western tropical Pacific.

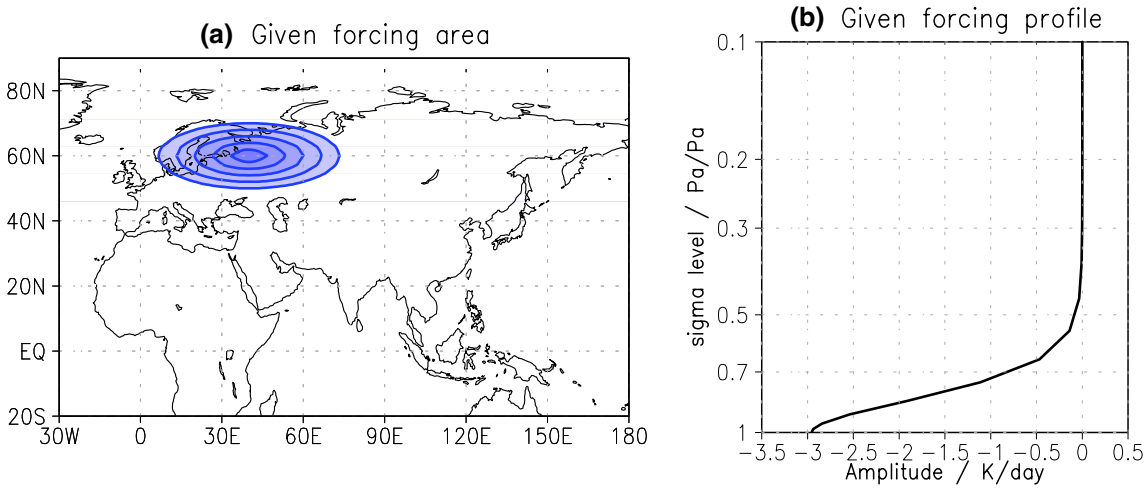

Fig. 8 **a** Horizontal distribution of the cooling anomaly from the *ANOM* run at the surface. Abscissa and ordinate are longitude and latitude, respectively. Contour interval is -0.5 K day^{-1} starting with -0.5 K day^{-1}. **b** Vertical profile of the cooling anomaly at 40°E and 60°N

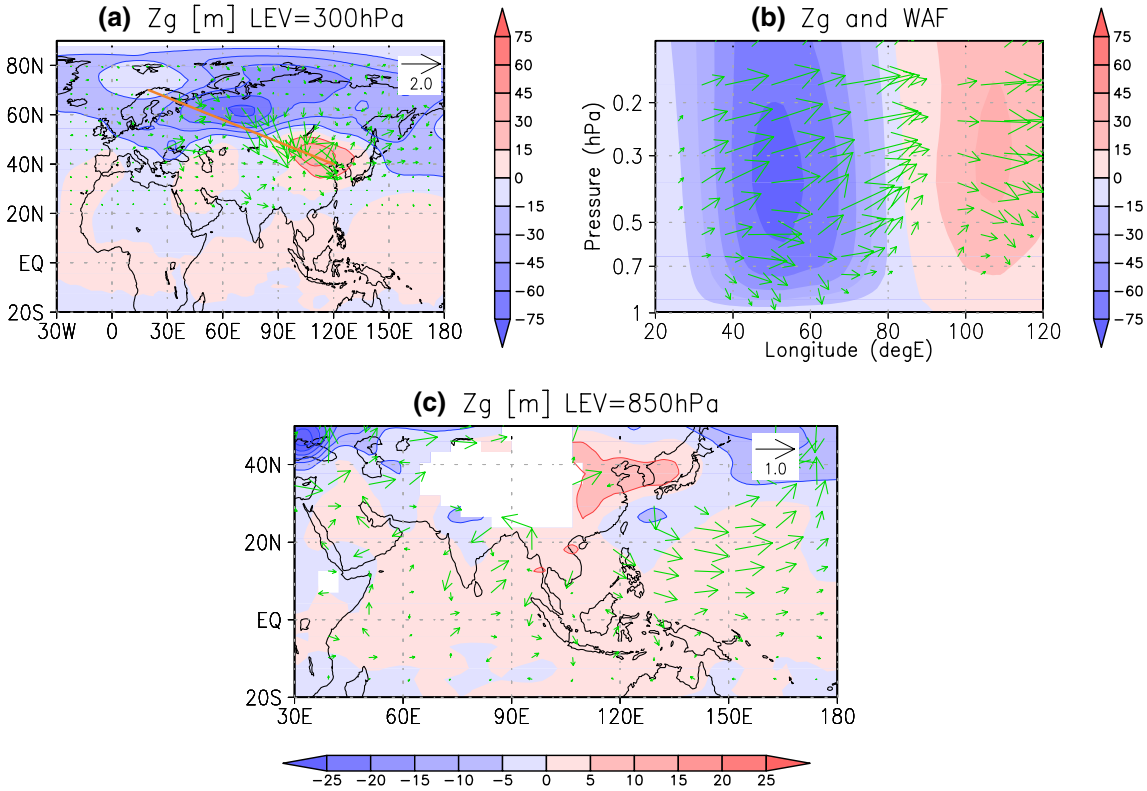

Fig. 9 **a** Geopotential height anomalies (*ANOM* minus *CNTL*) at 300 hPa averaged over the 30-day simulation run. Corresponding wave activity flux is shown by the *green arrows*. *Arrow* length corresponding to 2.0 m^2 s^{-2} is shown in the *upper right-hand corner* of the panel. Abscissa and ordinate are longitude and latitude, respectively. **b** Vertical cross section of geopotential height anomaly along the *brown line* in *panel* (**a**). *Green arrows* indicate vectors of zonal and vertical components of corresponding wave activity flux. The scale of the vectors is the same as in panel (**a**) but the vertical component was multiplied by a factor of 400. **c** As in panel (**a**), but for 850 hPa. *Arrows* indicate vectors of the horizontal wind anomaly. *Arrow* length corresponding to 1.0 m s^{-1} is shown in the *upper right-hand corner* of the panel

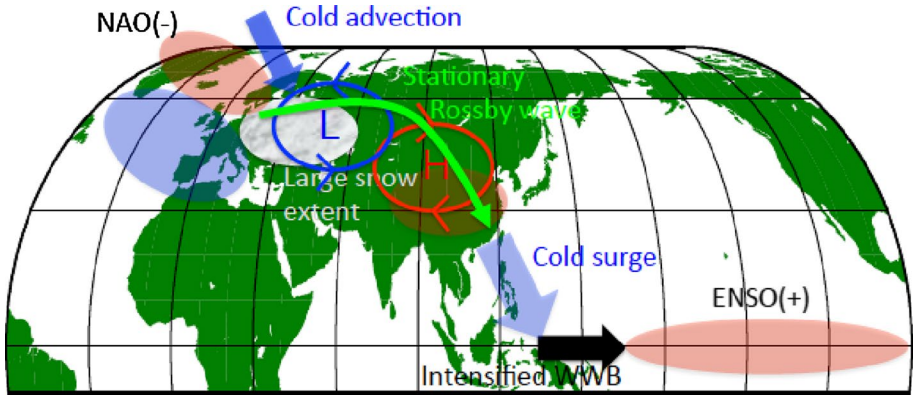

Fig. 10 A schematic diagram showing a possible mechanism that explains the 1-year-lagged relationship between the winter NAO and El Niño in the following year during the summer-to-winter time interval

4.3 Possible mechanisms

On the basis of the linear regression analysis results for the 16 CMIP3 models, in which only fields that had high coherency between the winter NAO and 1-year-lagged ENSO were used, we hypothesized that the snow anomalies over western Russia were associated with the NAO and remotely influenced the near-surface pressure fields over the Tibetan plateau via propagation of a stationary Rossby wave. An idealized experiment using a NLBM was performed to examine the remote influence of the snow anomaly on the near-surface pressure fields over the Tibetan plateau. This experiment showed a wave train-like pattern over Eurasia similar to the hypothesized Rossby wave. The surface wind fields in the western tropical Pacific obtained from NLBM show different wind direction and amplitude from those by the CMIP3, although some agreement among them are found, that is, the westerly anomalies over the western tropical Pacific and off-equatorial cyclonic anomalies. A reason of this will be discussed in the next section. We then hypothesized a possible mechanism for the 1-year-lagged relationship between the NAO and ENSO in Fig. 10 as follows:

- In association with the negative (positive) phase of the NAO in winter, larger (smaller) amounts of snow fall in eastern Europe/western Russia. Snow anomalies persist and gradually move northeastward during the transition of the seasons from winter to early spring.
- Larger (smaller) amounts of snow cool (warm) the atmosphere near the surface, and the resultant stationary Rossby wave response to the cooling induces a cyclonic (anticyclonic) anomaly over that region.
- A downstream anticyclonic (cyclonic) anomaly over the Tibetan plateau induces a relatively high (low) surface pressure anomaly over southeastern Asia through the induction of a low-level wind anomaly by the upper-level geopotential anomaly (Lau and Holopainen 1984; Lau and Nath 1991). The higher (lower) surface pressure anomaly intensifies (weakens) the Asian cold surge that intrudes into the equatorial warm pool region.
- Because of equatorward transport of the cold/dry air and higher planetary vorticity, cold surges reaching the tropics often generate off-equatorial cyclones north of the equator, which intensify WWBs (Yu and Rienecker 1998; Yu et al. 2003; Wang et al. 2011).
- The WWBs intensified by the surges initiate an El Niño in the early spring. Once the El Niño is initiated, the tropical convective region and associated warm SST region gradually move eastward as a result of air–sea interactions in the tropics (i.e., Bjerknes feedback). Consequently, an El Niño outbreak occurs several months later.

5 Discussion

In the initiation during boreal spring, the anomalous westerly wind in the western tropical Pacific excites intra-seasonal, oceanic Kelvin waves that induce warming of SST in the central-eastern tropical Pacific. Warming of SST then continues for several months and is accompanied by an eastward extension of the anomalous westerly wind, the result being formation of an El Niño-like SST pattern in the following summer to winter. During this development from spring to winter, the SST-warming anomalies are sustained by the westerly wind anomaly and in turn enhance the westerly wind in the western tropical Pacific, a mechanistic process known as positive Bjerknes feedback. We demonstrated that the winter NAO affects WWBs remotely and thus has an impact on ENSO variation. However, it should be noted that the WWB intensified remotely by the NAO initiates El Niño in a stochastic rather than a deterministic manner. Therefore, the winter NAO does not have a deterministic influence on ENSO. Because our CI analysis and regressions are based on linear relationships, the results also show a relationship between a positive NAO and a

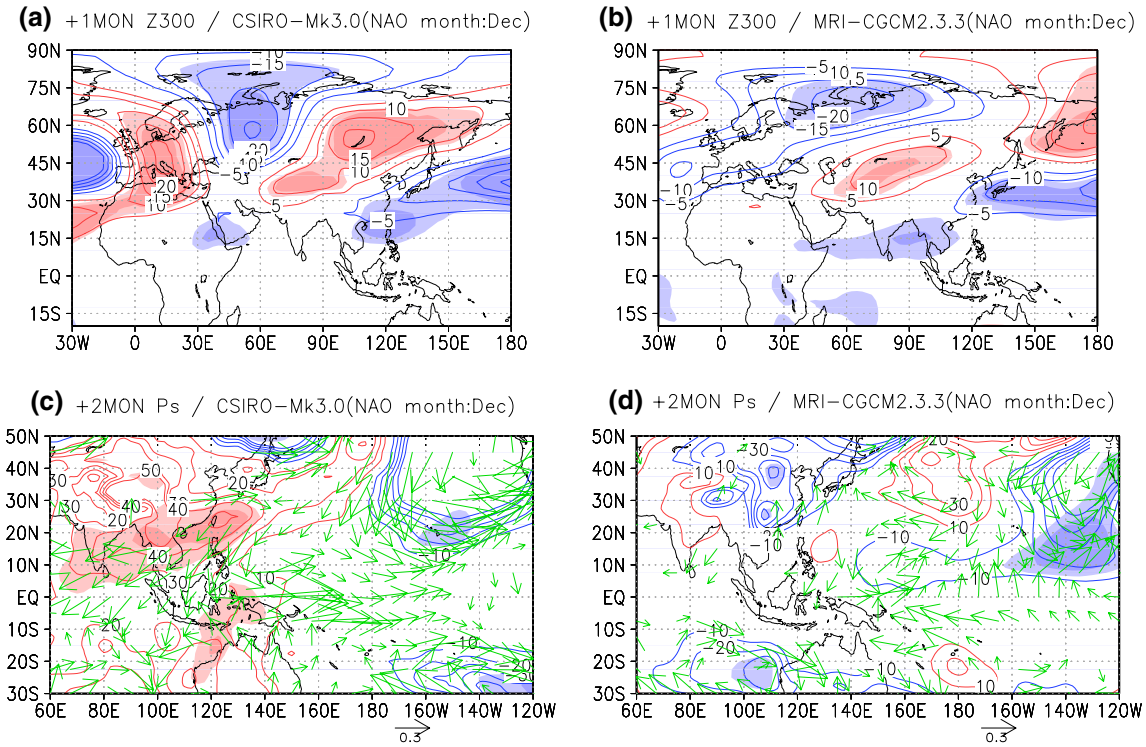

Fig. 11 Lag-regression anomalies of **a** Z300 (m) 1 month after (+1 MON) the NAO month, and **c** surface pressure (Pa) 2 months after the NAO month. The anomalies were obtained from the fields by linear regression on the $\mathbf{T}_A$ values of December of the NAO-month in CSIRO-Mk3.0. *Contour* indicates the regression coefficients. *Light* and *heavy red* (*blue*) *color* indicates positive (*negative*) anomalies with statistical significance exceeding 95 and 99 %, respectively. *Green arrows* drawn in *panel* (**c**) indicate vectors of surface wind anomalies. **b**, **d** Same as (**a**) and (**c**) but for December of the NAO-month in MRI-CGCM2.3.3

1-year-lagged La Niña, a relationship also demonstrated in Part I. It can be hypothesized that WWBs weakened remotely by a positive NAO decrease the probability of an El Niño's being initiated.

The WWBs are a key factor in the atmospheric forcing that initiates an El Niño. Seiki et al. (2011) have examined the extent to which the relationship between WWBs and ENSO are reproducible using CMIP3 models. The second column of Table 1 shows the reproducibility of the results of the models examined by them. There seems to be no clear correspondence to the CI values (third column). Seven CI values exceed the criterion of 0.5 in models evaluated as "Acceptable" or "Good", but 21 CI values exceed 0.5. However, if we consider only the observational results of the NAO during December, the number of CI values exceeding 0.5 is 3 for models evaluated as "Acceptable" (CNRM-CM3 and CSIRO-Mk3.0) or "Good" (MRI-CGCM2.3.3), and the total for all models is 5. Moreover, most CIs exceeding 0.5 are found in the early winter (i.e., November and December) for models evaluated as "Acceptable" or "Good". This finding seems reasonable, because winter-to-spring Eurasian snow anomalies are dominated by an early-winter rather than a late-winter NAO phase (Hori and Yasunari 2003).

The amplitudes of the ensemble mean westerly wind anomalies associated with WWB are weak (maximum is about 1.0 m s^{-1}). This is because the amplitudes of the anomaly of the ensemble mean are attenuated by the different locations of the response, which depends on the model. As examples of different responses between different models, single-model lag-regressions in CSIRO-Mk3.0 and MRI-CGCM2.3.3 are shown in Fig. 11. In CSIRO-Mk3.0 wave-train responses in Z300 are found as a negative anomaly in western Russia and positive around Lake Baikal (Fig. 11a). In MRI-CGCM2.3.3 wave-train responses appear as a negative anomaly on the Russian Arctic coast and as a positive anomaly north of the Tibetan Plateau (Fig. 11b). The amplitude of the anomaly of each model is larger (e.g., −25 m in CSIRO-Mk3.0 and −20 m in MRI-CGCM2.3.3 for the negative anomaly of Z300) than the ensemble mean (−3.6 m in Fig. 5b). Because the locations of the wave-train responses of the two models differ slightly, the superposition of the two waves results in attenuation of the amplitudes. However, physical linkage between the cold surface temperature in Europe/western Russia and the associated wave-train responses are commonly found in the different models. The amplitudes of the equatorial westerly wind anomalies are not larger in the two

models than the ensemble mean. Maxima are 0.7 m s^{-1} at 135°E in CSIRO-Mk3.0 (Fig. 11c) and 0.5 m s^{-1} at 145°E in MRI-CGCM2.3.3 (Fig. 11d). The intensity of westerly wind due to WWB was stronger (exceeding 10 m s^{-1}) if it was observed instantaneously or on a daily mean timeframe. However, the magnitudes of the monthly mean westerly wind anomalies during spring, which are related to an initiation ENSO, are a few m s^{-1} (e.g., Yu et al. 2003; Nakamura et al. 2006; Wang et al. 2011). Thus, the equatorial westerly wind anomalies obtained from the ensemble mean along with the individual models are not so weak as compared with observations.

We used the idealized model simulation in Sect. 4.2 to demonstrate the responses of the atmosphere to forcing associated with the cooling in Eastern Europe/western Russia related to the snow anomaly. The results qualitatively supported the CMIP3 (Sect. 4.1) and observation results (Part I). However, there were some inconsistencies among the models. In particular, the resultant surface wind anomaly in the western tropical Pacific did not directly correspond with the WWB. Whereas the CMIP3 results showed the westerly anomaly concentrated at the equator (Fig. 5c), the idealized model simulation showed a broad northwesterly anomaly north of the western tropical Pacific (Fig. 9c, around 130°E, 0°–20°N). This might be due to lack of air–sea interactions in the idealized model (i.e., Bjerknes feedback mechanism). However, because WWBs are intensified by background westerly wind anomalies, this result suggests that the forcing associated with cooling in Europe can influence the tropical Pacific without any feedback from ocean variations.

As we mentioned before, it is possible that many processes in addition to those addressed in this study cause the NAO–ENSO linkage. In the peak season of ENSO the tropical Pacific SST anomaly significantly impacts atmospheric circulation anomalies over the North Atlantic via the PNA pattern (e.g., Enfield and Mayer 1997; Klein et al. 1999; Saravanan and Chang 2000) or the stratospheric pathway (Scaife et al. 2005; Cagnazzo and Manzini 2009). The relevance of such concurrent effects from ENSO to NAO to the 1-year-lagged NAO–ENSO relationship may be problematic, at least considering the linear response of the system to ENSO. However, ENSO itself and its impacts on the atmosphere are nonlinear. For example, both in the beginning phase of El Niño and in the peak phase of La Niña, the tropical convection that strengthens anomalously in the western tropical Pacific often induces a negative PNA pattern. If the near-zero tropical SST anomaly in the concurrent winter of NAO (i.e., on the +0 m line in Fig. 3b) were a composite reflection of the beginning of El Niño and the end of La Niña, a negative PNA might be induced as a non-linear response to ENSO. Such an hypothesis about the non-linear response to ENSO could be applied to the stratospheric pathway. However, in the 16 CMIP-3 models used in this study only CNRM-CM3 (model top is 0.05 hPa/75 km) has a model top sufficiently high to simulate stratospheric variability. The other models have low tops (lower than 1.0 hPa). Furthermore, only the CNRM-CM3 and MRI-CGCM2.3.3 have more than three levels above 10 hPa (Cordero and Forster 2006). We therefore consider that most models did not simulate stratospheric variability. Thus present study did not take the roles of the stratosphere into account. Furthermore, attributions of both the NAO and ENSO to MJO-related anomalies in the tropics (Zavala-Garay et al. 2005; Cassou 2008; Lin et al. 2009) might explain part of the remote and delayed linkage between NAO and ENSO. Although the fidelity of the behavior of the MJO simulated by CMIP3 models to observations is not very good (Lin et al. 2006), it is noteworthy that the CNRM-CM3 and ECHAM5/MPI-OM models, which Lin et al. (2006) have remarked to do the best job of simulating the MJO among the CMIP3 models, showed a high CI with the December NAO (Table 1). Considering the role of the MJO in the NAO–ENSO relationship, applying the CI analysis to CMIP-5 models that exhibit an overall improvement over the CMIP3 models in the simulation of tropical intra-seasonal variability (Hung et al. 2013) might be one approach to deepening understanding of this issue.

6 Summary

This study was carried out to complement the observational evidence presented in Part I that a winter NAO precedes an ENSO during the second half of the following year, and to identify a possible mechanism underlying the relationship between the NAO and ENSO by use of a multi-model analysis with a coupled atmosphere–ocean climate model. We developed an index, the CI, which is a measure of the coherence between the NAO and ENSO in a particular model. Selection of CMIP3 models with positive CI values made it possible to reproduce the observed 1-year-lagged relationship between the NAO and ENSO in the coupled models. Multi-model ensemble means of the regression fields associated with the negative phase of the NAO revealed the important role of Eurasian snow anomalies in the remote influence of the NAO on modification of the WWB in the western tropical Pacific region. An ideal model experiment using a NLBM, similar to a dry AGCM, supported the remote influence of the NAO on the western tropical Pacific via Eurasian snow anomalies. The inconsistency between the idealized model and CMIP3 results suggested the importance of air–sea interactions to enhancement of WWBs. Anomalous fields obtained from multi-model ensemble means of CMIP3 models agreed with the observational results shown in Part I. We therefore established that the CI is a useful tool for quantifying the

physical linkage between two phenomena, even if they are separated spatially and temporally.

In this study, we focused on the influences of the NAO on ENSO. In general, however, influences of tropical variability on the extra-tropics are more obvious. In fact, because ENSO has a characteristic period of 4 years, we cannot rule out the possibility that the winter NAO is excited by the remote influence of an El Niño during the previous year. Yasunari (1987) and Barnett et al. (1989) have proposed that the NAO and Eurasian snow might be a part of what constitutes the ENSO cycle. However, clear understanding of the contribution of extra-tropical variabilities on such a global scale has not yet been obtained. Our results might help improve understanding of such a global cycle.

Acknowledgments We thank K. Yamazaki and J. Ukita for their useful discussions. We also thank three anonymous reviewers for their valuable remarks to improve the quality of the paper. We acknowledge the modeling groups, the Program for Climate Model Diagnosis and Intercomparison (PCMDI) and the WCRP's Working Group on Coupled Modeling (WGCM), for their roles in making available the WCRP CMIP3 multi-model dataset. Support of this dataset is provided by the Office of Science, U.S. Department of Energy. The NLBM we used was provided by M. Watanabe (Atmospheric and Ocean Research Institute, the University of Tokyo). This study was supported by the "Green Network of Excellence" Program (GRENE Program) of the Arctic Climate Change Research Project and Japanese Ministry of Education, Culture, Sports, Science and Technology (MEXT) through a Grant-in-Aid for Scientific Research in Innovative Areas 2205.

References

Barnett TP, Dumenil L, Schlese V, Roeckner E, Latif M (1989) The effect of Eurasian snow cover on regional and global climate variations. J Atmos Sci 46:661–685

Cagnazzo C, Manzini E (2009) Impact of the stratosphere on the winter tropospheric teleconnections between ENSO and the North Atlantic and European Region. J Clim 22:1223–1238

Cassou C (2008) Intraseasonal interaction between the Madden–Julian Oscillation and the North Atlantic Oscillation. Nature 455:523–527

Chen S, Yu B, Chen W (2014) An analysis on the physical process of the influence of AO on ENSO. Clim Dyn 42:973–989. doi:10.1007/s00382-012-1654-z

Chung C, Nigam S (1999) Weighting of geophysical data in principal component analysis. J Geophys Res 16:925–928

Cordero EC, Forster PM (2006) Stratospheric variability and trends in models used for the IPCC AR4. Atmos Chem Phys 6:5369–5380. doi:10.5194/acp-6-5369-2006

Enfield DB, Mayer DA (1997) Tropical Atlantic sea surface temperature variability and its relation to El Niño–Southern Oscillation. J Geophys Res 102:929–945

Giese BS, Harrison DE (1990) Aspects of the Kelvin wave response to episodic wind forcing. J Geophys Res 95:7289–7312

Gill AE (1980) Some simple solutions for heat-induced tropical circulation. Q J R Meteorol Soc 106:447–462

Ham YG, Kug JS, Park JY, Jin FF (2013) Sea surface temperature in the north tropical Atlantic as a trigger for El Niño/Southern Oscillation events. Nat Geosci 6:112–116. doi:10.1038/ngeo01686

Handorf D, Dethloff K (2012) How well do state-of-the-art atmosphere–ocean general circulation models reproduce atmospheric teleconnection patterns? Tellus A 64:19777. doi:10.3402/tellusa.v64i0.19777

Horel JD, Wallace JM (1981) Planetary-scale atmospheric phenomena associated with the Southern Oscillation. Mon Weather Rev 109:813–829

Hori ME, Yasunari T (2003) NAO impact towards the springtime snow disappearance in the western Eurasian continent. Geophys Res Lett 30(19):1977. doi:10.1029/2003GL018103

Hung MP, Lin JL, Wang W, Kim D, Shinoda T, Weaver SJ (2013) MJO and convectively coupled equatorial waves simulated by CMIP5 climate models. J Clim 26:6185–6214. doi:10.1175/JCLI-D-12-00541.1

Kalnay E et al (1996) The NCEP/NCAR 40-year reanalysis project. Bull Am Meteorol Soc 77:437–471

Kindle JC, Phoebus PA (1995) The ocean response to operational westerly wind bursts during the 1991–1992 El Niño. J Geophys Res 100:4893–4920

Klein SA, Soden BJ, Lau NC (1999) Remote sea surface temperature variations during ENSO: evidence for a tropical atmospheric bridge. J Clim 12:917–932

Kosaka Y, Chowdary JS, Xie SP, Min YM, Lee JY (2012) Limitations of seasonal predictability for summer climate over East Asia and the Northwestern Pacific. J Clim 25:7574–7589. doi:10.1175/JCLI-D-12-00009.1

Lau NC, Holopainen EO (1984) Transient eddy forcing of the time-mean flow as identified by geopotential tendencies. J Atmos Sci 41:313–328

Lau NC, Nath MJ (1991) Variability of the baroclinic and barotropic transient eddy forcing associated with monthly changes in the midlatitude storm tracks. J Atmos Sci 48:2589–2613

Lin JL et al (2006) Tropical intraseasonal variability in 14 IPCC AR4 climate models. Part I: convective signals. J Clim 19:2665–2690

Lin H, Brunet G, Derome J (2009) An observed connection between the North Atlantic Oscillation and the Madden–Julian oscillation. J Clim 22:364–380

Matsuno T (1966) Quasi-geostrophic motions in the equatorial area. J Meteorol Soc Jpn 44:25–42

Meehl GA et al. (2007) Global climate projections. In: Solomon et al. (ed) Climate change 2007 The Physical Science Basis, Contribution of Working Group I to the Fourth Assessment Report of the Intergovernmental Panel on Climate Change. Cambridge Univ Press, New York, pp 748–849

Randall DA et al (2007) Climate models and their evaluation. In: Solomon et al (ed) Climate Change 2007 The Physical Science Basis, Contribution of Working Group I to the Fourth Assessment Report of the Intergovernmental Panel on Climate Change. Cambridge Univ Press, New York, pp 590–662

Nakamura T, Tachibana Y, Honda M, Yamane S (2006) Influence of the Northern Hemisphere annular mode on ENSO by modulating westerly wind bursts. Geophys Res Lett 33:L07709. doi:10.1029/2005GL025432

Nakamura T, Tachibana Y, Shimoda H (2007) Importance of cold and dry surges in substantiating the NAM and ENSO relationship. Geophys Res Lett 34:L22703. doi:10.1029/2007GL031220

Ohba M, Nohara D, Ueda H (2010) Simulation of asymmetric ENSO transition in WCRP CMIP3 multimodel experiments. J Clim 23:6051–6067. doi:10.1175/2010JCLI3608.1

Onogi K et al (2007) The JRA-25 reanalysis. J Meteorol Soc Jpn 85:369–432. doi:10.2151/jmsj.85.369

Oshika M, Tachibana Y, Nakamura T (2014) Impact of the winter North Atlantic Oscillation (NAO) on the Western Pacific (WP) pattern in the following winter through Arctic sea ice and ENSO: part I—observational evidence. Clim Dyn. doi:10.1007/s00382-014-2384-1

Peings Y, Douville H (2010) Influence of the Eurasian snow cover on the Indian summer monsoon variability in observed climatologies and CMIP3 simulations. Clim Dyn 34:643–660. doi:10.1007/s00382-009-0565-0

Philander SG (1985) El Niño and La Niña. J Atmos Sci 42:2652–2662

Roesch A (2006) Evaluation of surface albedo and snow cover in AR4 coupled climate models. J Geophys Res 111:D15111. doi:10.1029/2005JD006473

Saravanan R, Chang P (2000) Interaction between tropical Atlantic variability and El Niño–Southern oscillation. J Clim 13:2177–2194

Scaife AA, Knoght JR, Vallis GK, Folland CK (2005) A stratospheric influence on the winter NAO and North Atlantic surface climate. Geophys Res Lett 32:L18715. doi:10.1029/2005GL023226

Seiki A, Takayabu YN, Yasuda T, Sato N, Takahashi C, Yoneyama K, Shirooka R (2011) Westerly wind bursts and their relationship with ENSO in CMIP3 models. J Geophys Res 116:D03303. doi:10.1029/2010JD015039

Stoner AMK, Hayhoe K, Wuebbles DJ (2009) Assessing general circulation model simulations of atmospheric teleconnection patterns. J Clim 22:4348–4372. doi:10.1175/2009JCLI2577.1

Takaya K, Nakamura H (2001) a formulation of a phase-independent wave-activity flux for stationary and migratory quasigeostrophic eddies on a zonally varying basic flow. J Clim 58:608–627

Thompson DWJ, Wallace JM (1998) The Arctic Oscillation signature in the wintertime geopotential height and temperature fields. Geophys Res Lett 25:1297–1300

Von Storch H, Zwiers FW (1999) Statistical analysis in climate research. Cambridge University Press, Cambridge

Wallace JM, Gutzler DS (1981) Teleconnections in the geopotential height field during the Northern Hemisphere winter. Mon Weather Rev 109:784–812

Wang X, Wang C, Zhou W, Wang D, Song J (2011) Teleconnected influence of North Atlantic sea surface temperature on the El Niño onset. Clim Dyn 37:663–676. doi:10.1007/s00382-010-0833-z

Xie SP, Hu KM, Hafner J, Tokinaga H, Du Y, Huang G, Sampe T (2009) Indian Ocean capacitor effect on Indo–Western Pacific Climate during the summer following El Nino. J Clim 22:730–747

Yasui S, Watanabe M (2010) Forcing processes of the summertime circumglobal teleconnection pattern in a dry AGCM. J Clim 23:2093–2114

Yasunari T (1987) Global structure of El Niño/Southern Oscillation. Part II time evolution. J Meteorol Soc Jpn 65:81–102

Yasunari T, Kitoh A, Tokioka T (1991) Local and remote responses to excessive snow mass over Eurasia appearing in the Northern spring and summer climate. J Meteorol Soc Jpn 69:473–487

Yu L, Rienecker MM (1998) Evidence of an extratropical atmospheric influence during the onset of the 1997–1998 El Niño. Geophys Res Lett 25:3537–3540

Yu L, Weller RA, Liu WT (2003) Case analysis of a role of ENSO in regulating the generation of westerly wind bursts in the Western Equatorial Pacific. J Geophys Res 108(C4):3128. doi:10.1029/2002JC001498

Zavala-Garay J, Zhang C, Moore AM, Kleeman R (2005) The linear response of ENSO to the Madden–Julian oscillation. J Clim 18:2441–2459